

Emergent broadband polarization entanglement from electronic and phononic four-wave mixing indistinguishability

Diego Sier^{1,4}, Lucas Valente^{1,4}, Tiago A. Freitas², Marcelo F. Santos³, Carlos H. Monken¹, Raul Corrêa², and Ado Jorio^{1*}

¹*Departamento de Física, Universidade Federal de Minas Gerais, Belo Horizonte, MG 30123-970, Brazil*

²*IDOR/Pioneer Science Initiative, Rio de Janeiro, RJ 22281-010, Brazil*

³*Instituto de Física, UFRJ, Rio de Janeiro, RJ 21941-972, Brazil and*

⁴*These two authors contributed equally.*

(Dated: August 22, 2024)

Abstract

Recently [*PRA* **108**, L051501 (2023)], it has been shown that in a centrosymmetric cubic system, two-photons from a broadband intense laser field can be converted into a pair of Stokes and anti-Stokes entangled photons. Here we properly explain, demonstrate, quantify (for diamond) and explore the possibilities offered by such system, designing an entanglement map based on changes in the light-matter system. In particular, we show how the broadband polarization entanglement, that emerges from the interference between electronic and phononic degrees of freedom in the four-wave mixing process, depends on parameters such as Stokes-anti-Stokes Raman shift, scattering geometry and laser bandwidth, opening the avenue of exploration of such phenomenon in information processing.

The operation of converting incoming photon(s) into different outgoing photon(s) in a medium is dictated by its susceptibility χ [1, 2]. In centrosymmetric materials, the second-order susceptibility is null and the non-linear response is usually dominated by the third-order tensor [3]. The $\chi^{(3)}$ enables two photons from a broadband intense laser field to interact with the medium to produce Stokes and anti-Stokes shifted quanta ($\hbar\omega_L + \hbar\omega'_L = \hbar\omega_S + \hbar\omega_{aS}$), known as the SaS photon pair [4–6]. While the non-classical correlations between SaS photons have been widely established [7–11], the presence of polarization entanglement in such fundamental four-wave mixing process has been demonstrated only very recently, in diamond [12].

This recent result indicates that the fundamental four-wave mixing (FWM) polarization entanglement comes from the indistinguishability between electronic (e-FWM) and phononic (p-FWM) mediated processes inside the centrosymmetric material. It should, therefore, be possible to tailor the SaS state by playing with state preparation parameters, such as the scattering geometry, the SaS Raman shift and the laser bandwidth [13–15]. In fact, the interplay of the SaS scattering properties should generate a map of different degrees of polarization entanglement depending on the balance between the electronic and phononic degrees of freedom. Properly demonstrating, quantifying and exploring these possibilities is the goal of this paper.

The correlated SaS scattered intensity can be obtained by the electric polarization in the

material [1, 2]

$$P_i(\omega_{aS}) \propto \chi_{ijkl}^{(3)}(-\omega_{aS}, \omega_L, \omega'_L, -\omega_S) \mathcal{E}_j(\omega_L) \mathcal{E}_k(\omega'_L) E_l^\dagger(\omega_S), \quad (1)$$

where \mathcal{E} and E represent the laser and scattered modes, respectively, and indexes $\{i, j, k, l\}$ represent polarization directions. The laser modes are occupied by an intense classical field, which is unaffected by the scattering of a few photons, while the Stokes and anti-Stokes modes start in the vacuum. The incident laser spectral amplitude is written as $\mathcal{E}_j(\omega_L) = \mathcal{E}_{0j} G(\omega_L)$, $G(\omega_L)$ describing the laser spectral distribution with $\int_0^\infty |G(\omega_L)|^2 d\omega_L = 1$. The probability amplitude that describes the SaS pair scattered at frequencies ω_S and ω_{aS} in a polarization pure state $|\psi\rangle$ is obtained by calculating $\langle 0|E_l(\omega_S)E_i(\omega_{aS})|\psi\rangle + \langle 0|E_i(\omega_{aS})E_l(\omega_S)|\psi\rangle$ [16], and the two-photon scattering amplitude probability at the same frequencies reads

$$\begin{aligned} \Psi_{li}(\omega_S, \omega_{aS}) = & C \mathcal{E}_{0j} \mathcal{E}_{0k} \int_{-\omega_S}^{\infty} G(\omega_S + \omega) G(\omega_{aS} - \omega) \\ & \times \left[A_{ijkl}^E + A_{ijkl}^R \frac{\gamma}{\omega_{ph} - \omega + i\gamma/2} \right] d\omega, \end{aligned} \quad (2)$$

where the total FWM susceptibility (in brackets) is composed of a constant electronic and a resonant phononic component [1, 2, 14].

The diamond structure belongs to the O_h point group [13, 14]. In this case, $\chi_{ijkl}^{(3)}$ has only four independent terms [3], which are $\chi_{xxxx}^{(3)}$, $\chi_{xxyy}^{(3)}$, $\chi_{xyxy}^{(3)}$, $\chi_{xyyx}^{(3)}$ (assuming light propagating in the z direction and that the x and y directions coincide with the crystallographic axes). The frequency dispersion of the electronic contribution e-FWM can be neglected when it is very far from any electronic resonance, so that $\chi_{ijkl}^{(3)E}(-\omega_{aS}, \omega_L, \omega'_L, -\omega_S) = A_{ijkl}^E \delta(\omega_L + \omega'_L - \omega_S - \omega_{aS})$ becomes a complex constant tensor fulfilling energy conservation. Ideally, the ratio between the e-FWM components in centrosymmetric materials is $\chi_{xxxx}^{(3)E} \approx 3\chi_{xxyy}^{(3)E} \approx 3\chi_{xyxy}^{(3)E} \approx 3\chi_{xyyx}^{(3)E}$ [1]. However, experimental conditions are rarely ideal and we will only take these values as a reference.

The p-FWM susceptibility tensor, on the other hand, is known to be $\chi_{ijkl}^{(3)R} \propto \sum_{\sigma} (\alpha_{ij,\sigma}^R \alpha_{kl,\sigma}^R + \alpha_{ik,\sigma}^R \alpha_{jl,\sigma}^R)$ [13], where $\alpha_{ij,\sigma}^R$ is the polarizability Raman tensor that describes the scattering of an incident electric field polarized at i into a scattered mode polarized at j , via a phonon σ . The Raman active vibrational mode of diamond belongs to the T_{2g} irreducible representation of the O_h point group. Due to the relatively small probability of formation

of SaS pairs, the spectral features of the phononic contribution to the susceptibility can be calculated from perturbation theory [1], and A_{ijkl}^R in Eq. (2) is the tensorial part of $\chi_{ijkl}^{(3)R}$. The frequency dependence is composed of a Lorentzian-shaped amplitude of the Stokes scattering phonon frequency, $\omega = \omega_L - \omega_S$, around the resonance ω_{ph} with width $\gamma/2$ (γ is the phonon decay rate, inversely proportional to its lifetime). This susceptibility is the same as when the scattered fields are classical [1, 2], being an extrapolation of the stimulated Raman scattering to the regime where the Stokes stimulation is turned off.

The SaS scattering amplitude is widened by the laser bandwidth, which adds an energy uncertainty to the scattered photons in both electronic and phononic processes. The factor C in Eq. (2) contains the efficiency of the FWM scattering in polarizations l (Stokes) and i (anti-Stokes), and depends on the scattered field frequencies and the scattering angles. However, we can consider C a constant in our experiments because we only collect pairs in forward scattering and because the laser bandwidth and phonon spectrum, taken care separately in Eq. (2), dominate any other frequency dependence. Assuming a Gaussian amplitude spectrum for the laser, $G(\omega_L) = (\pi W^2)^{-1/4} e^{-(\omega_L - \omega_c)^2 / 2W^2}$, centered around the angular frequency ω_c with width W (the laser power spectrum FWHM is $2\sqrt{\ln 2}W / (2\pi)$), the integral (2) can be solved analytically.

With the probability amplitude (2) we can construct the SaS two-photon state generated by this FWM process. We assume the laser polarization to be vertical (V) with respect to the laboratory, denoted by \hat{e}_V . If the crystallographic axis x is also along the vertical direction, then $\hat{e}_V = \hat{x}$, and the susceptibility $\chi_{ixxl}^{(3)}$ will govern the photon pair production. In general, however, if the crystallographic axis x and the laser polarization have an angle θ between them, such that $\hat{e}_V = \cos(\theta)\hat{x} + \sin(\theta)\hat{y}$, there will be a coherent sum of certain components of the susceptibility tensor defining the scattered photons polarization. By writing the laser field components as $\mathcal{E}_{0x} = \mathcal{E}_0 \cos \theta$ and $\mathcal{E}_{0y} = \mathcal{E}_0 \sin \theta$, the scattered (non-normalized) state can be written as

$$\begin{aligned}
|\Psi_{SaS}\rangle(\omega_S, \omega_{aS}; \theta) &= [Y_{VV}^E(\theta)f^E + Y_{VV}^R(\theta)f^R]|VV\rangle \\
&\quad + [Y_{HH}^E(\theta)f^E + Y_{HH}^R(\theta)f^R]|HH\rangle \\
&\quad + [Y_{VH}^E(\theta)f^E + Y_{VH}^R(\theta)f^R](|VH\rangle + |HV\rangle),
\end{aligned} \tag{3}$$

where $f^\eta(\omega_S, \omega_{aS})$ carries the spectral dependence of the scattering for $\eta = \{E, R\}$, being

$f^E \equiv e^{-\bar{\omega}^2/W^2}$ and

$$f^R \equiv e^{-\bar{\omega}^2/W^2} \frac{\gamma e^{-(\Omega - i\gamma/2)^2/W^2}}{2i\sqrt{\pi}W} \operatorname{erfc} \left(\frac{\gamma}{2W} + i \frac{\Omega}{W} \right), \quad (4)$$

with $\bar{\omega} \equiv (\omega_S + \omega_{aS})/2 - \omega_c$ and $\Omega \equiv (\omega_{aS} - \omega_S)/2 - \omega_{ph}$, and where $Y_{li}^\eta(\theta)$ are functions that depend on the angle θ and the A_{ijkl}^η tensor components,

$$Y_{VV}^\eta(\theta) \equiv C\mathcal{E}_0^2[(\mathcal{S}^4 + \mathcal{C}^4)A_{xxxx}^\eta + 2\mathcal{S}^2\mathcal{C}^2(A_{xyyx}^\eta + A_{xxyy}^\eta + A_{xyxy}^\eta)], \quad (5a)$$

$$Y_{HH}^\eta(\theta) \equiv C\mathcal{E}_0^2[2\mathcal{S}^2\mathcal{C}^2A_{xxxx}^\eta + (\mathcal{S}^4 + \mathcal{C}^4)A_{xyyx}^\eta - 2\mathcal{S}^2\mathcal{C}^2(A_{xxyy}^\eta + A_{xyxy}^\eta)], \quad (5b)$$

$$Y_{VH}^\eta(\theta) \equiv C\mathcal{E}_0^2(\mathcal{S}^2 - \mathcal{C}^2)\mathcal{S}\mathcal{C} \times (A_{xxxx}^\eta - A_{xyyx}^\eta - A_{xxyy}^\eta - A_{xyxy}^\eta), \quad (5c)$$

where $\mathcal{S} \equiv \sin \theta$ and $\mathcal{C} \equiv \cos \theta$. Equation (3) means that the angle θ drives the balance between the contribution of the e-FWM spectrum in f^E and the p-FWM spectrum in f^R , and this balance will be different for each pair of scattered photons polarization VV , HH and VH (equal to HV), depending on how the tensor components are combined.

The state in Eq. (3) is, in general, entangled in polarization. In particular, for $\theta = 0^\circ$, $Y_{VH}^\eta(0^\circ) = 0$, and $\{|VV\rangle, |HH\rangle\}$ form a Schmidt basis [17], meaning that if the amplitudes of these vector components are equal, state $|\Psi_{SaS}\rangle$ (3) is maximally entangled, while if one of them is zero, it is separable. In this sense, the problem of producing a state with a high amount of polarization entanglement becomes a matter of tailoring the relative amplitude of the two components of this Schmidt basis.

To obtain a prediction for the SaS state generated as a function of θ , one needs to characterize the tensor components A_{ijkl}^η in the functions $Y_{li}^\eta(\theta)$, Eq. (5). The functions f^η in Eq. (3) are known and only depend on the laser central frequency ω_c , bandwidth W , the phonon frequency ω_{ph} and decay rate γ , which are given experimental conditions. Measuring the relative scattered intensities into $|HH\rangle$ and $|VV\rangle$ in $\theta = 0^\circ$ and $\theta = 45^\circ$ (angles in which there are no $|VH\rangle$ and $|HV\rangle$ components) allows us to retrieve the values of A_{ijkl}^η . Next, we present an experiment that was used to extract these quantities in diamond, and show how they translate into SaS entanglement.

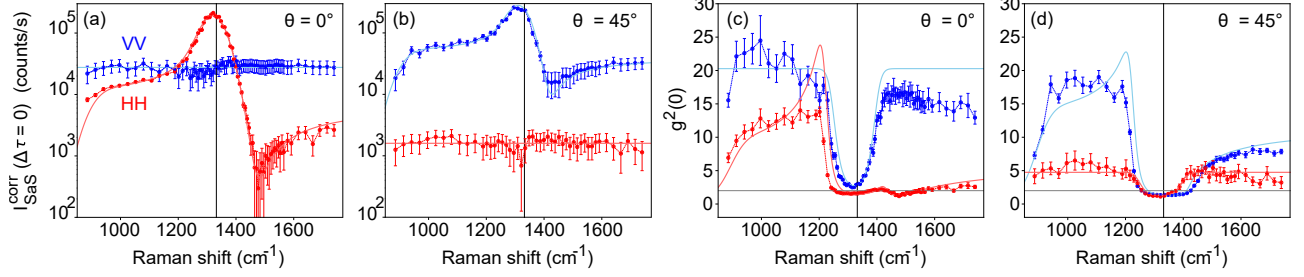


FIG. 1. (a,b) Time-correlated SaS photon pairs intensity at VV (blue dots) and HH (red dots) polarization, for crystallographic orientation at (a) $\theta = 0^\circ$ and (b) $\theta = 45^\circ$. The I_{SaS}^{corr} data was corrected to account for system efficiency and adjusted by the square of the laser power [18]. Lines are the theoretical model: the flat curves are the mean counts $\langle I_{SaS}^{corr} \rangle$ at VV(0°) and HH(45°); for the resonance curves, HH(0°) and VV(45°), $\omega_{ph}/2\pi = 1332 \text{ cm}^{-1}$, $\gamma = 11 \text{ cm}^{-1}$, $\omega_c/2\pi = 12.7 \times 10^3 \text{ cm}^{-1}$, and $W/2\pi = 42 \text{ cm}^{-1}$ in Eq. (2) [18]. The fitting Y factors from Eq. (3) were $Y_{HH}^E(0^\circ) = \langle I_{SaS}^{corr}(VV(0^\circ)) \rangle^{1/2}(0.68 - i0.12)$, $Y_{VV}^E(45^\circ) = \langle I_{SaS}^{corr}(VV(0^\circ)) \rangle^{1/2}(1.61 - i0.55)$, and $Y_{HH}^R(0^\circ) = Y_{VV}^R(45^\circ) = 51450$. (c,d) $g^{(2)}(0)$ values for a diamond crystallographic orientation of (c) 0° and (d) 45° . The light gray lines indicate the classical limit $g^{(2)} = 2$.

The experimental setup utilized is similar to the one described in [12], with the addition of a monochromator to filter the Stokes signal [18]. The polarization of the laser is vertical (V) with respect to the laboratory and, for each monochromator position (each selected $\delta\omega = \omega_c - \omega_S$), one histogram of temporal difference is obtained in 300 seconds of acquisition. This scanning procedure is done for two orientations of the sample ($\theta = 0^\circ$ and 45°), and for each sample orientation the spectrum is obtained with the polarization of the photons incident on the avalanche photodiode (APD) detectors being selected in two ways—a spectrum with Stokes and anti-Stokes photons with vertical polarization (VV) and a spectrum with both photons with horizontal polarization (HH). The sample utilized was a diamond grown by a CVD process (Type IIac, 100-oriented, from Almax) positioned so that the laser propagates in the (001) direction of the crystal.

The intensity spectra of correlated SaS pairs for VV (blue dots) and HH (red dots) polarization at $\theta = 0^\circ$ and $\theta = 45^\circ$ are displayed in Fig. 1 (a) and (b), respectively. According to group theory analysis, VV(0°) configuration does not exhibit a Raman contribution ($A_{xxxx}^R = 0$ in Eq. (5)) and only involves non-resonant electronic transitions. For this reason, the blue curve shown in Fig. 1 (a) corresponding to this configuration is flat. Additionally,

Fig. 1 (a) shows a light blue solid line, obtained by averaging the intensity values I_{SaS}^{corr} for this experimental configuration, $\langle I_{SaS}(VV(0^\circ)) \rangle = (27.5 \pm 3.5) \times 10^3$. Since $Y_{VV}^E(0^\circ) = C\mathcal{E}_0^2 A_{xxxx}^E$ and in our model it is proportional to $\langle I_{SaS}(VV(0^\circ)) \rangle^{1/2}$, we have a reference value for A_{xxxx}^E .

By looking at the other relevant scattering geometries, we obtain the other tensorial components of Eq. (5) in relation to A_{xxxx}^E . The HH(45°) configuration also exhibits only e-FWM, as seen in the red data in Fig 1 (b). The mean and standard deviation of the counts gives $(1.60 \pm 0.28) \times 10^3$. The HH(0°) data in Fig. 1 (a) (red points) contains p-FWM with the characteristic resonance signature, which comes from $A_{xyyx}^R \neq 0$ in Eq. (5b), contributing with a Raman scattering in the $|HH\rangle$ polarization. Using $Y_{HH}^E(0^\circ) = \langle I_{SaS}^{corr}(VV(0^\circ)) \rangle^{1/2}(0.68 - i0.12)$ and $Y_{HH}^R(0^\circ) = 51450$ fits the data with the shown theoretical curve in Fig. 1 (a). The VV(45°) data is the last configuration left, and it is shown in Fig. 1 (b) in blue. In order to fit it, we fix the Raman factor to be the same as in the HH(0°) configuration, $Y_{VV}^R(45^\circ) = 51450$, and use $Y_{VV}^E(45^\circ) = \langle I_{SaS}^{corr}(VV(0^\circ)) \rangle^{1/2}(1.61 - i0.55)$. With the above values and working with Eq. (5) we obtain the electronic and Raman A_{ijkl}^η components, summarized in Table I.

TABLE I. List of measured electronic and Raman tensor components ratios A_{ijkl}^η/A_{xxxx}^E [18].

Tensor component	Value
A_{xyyx}^E/A_{xxxx}^E	$(0.37 \pm 0.04) + i(-0.07 \pm 0.01)$
$(A_{xxyy}^E + A_{xyxy}^E)/A_{xxxx}^E$	$(0.89 \pm 0.010) + i(-0.07 \pm 0.01)$
A_{xxxx}^R/A_{xxxx}^E	0
A_{xyyx}^R/A_{xxxx}^E	(171 ± 12)
$(A_{xxyy}^R + A_{xyxy}^R)/A_{xxxx}^E$	(171 ± 12)

For completeness the second-order correlation function $g^{(2)}(0)$ is evaluated with the ratio $[I_{SaS}^{corr}(\Delta\tau = 0) + \bar{I}_{SaS}(\Delta\tau \neq 0)]/\bar{I}_{SaS}(\Delta\tau \neq 0)$, where $I_{SaS}^{corr}(\Delta\tau = 0)$ are the measurements in Fig. 1 (a) and (b), and $\bar{I}_{SaS}(\Delta\tau \neq 0)$ accounts for the uncorrelated pair production. A plot of $g^{(2)}(0)$ is shown in Fig. 1(c,d), where it is evident that near the resonance the values are the lowest, accounting for the high number of uncorrelated SaS photon pairs produced. Furthermore, the curves for HH(0°) and VV(45°) show a drop in $g^{(2)}(0)$, being higher below and lower above the resonance region, while the VV(0°) and HH(45°) keep roughly the same value. The asymmetry in HH(0°) and VV(45°) is associated with the uncorrelated

counts being symmetrical with respect to the resonance peak, and thus the asymmetry in the correlated counts for these configurations, which contain a p-FWM contribution, is transferred to the $g^{(2)}(0)$ curves. This asymmetry is a result of the constructive ($\delta\omega < \omega_{ph}$) versus destructive ($\delta\omega > \omega_{ph}$) interference between the e-FWM and the p-FWM, which explains the Cooper-pair-like behavior of I_{SaS} [10, 15]. On the other hand, the correlated counts in the VV(0°) and HH(45°) configurations are a purely e-FWM contribution, and thus are a flat curve, leading to an overall symmetric $g^{(2)}(0)$.

With the values of A_{ijkl}^n in hand, one can predict what is the entanglement in the SaS scattered state $|\Psi_{SaS}\rangle(\theta)$ of Eq. (3) for given values of ω_S and ω_{aS} . We use, as an entanglement measure, the entropy of entanglement $E = -\text{Tr}_i(\rho_i \log_2 \rho_i)$ of either subsystem $i = \{S, aS\}$ with reduced state ρ_i [17], which, since our global state is pure, is zero for separable states and unity for maximally entangled states.

In Fig. 2 we show a contour plot of $E(\omega_S, \omega_{aS}; \theta, W)$, under the condition that $\omega_{aS} = 2\omega_c - \omega_S$, that is, a symmetric SaS Raman shift. On the horizontal axis we vary the Raman shift, going through the resonance in diamond at $\omega_{ph}/2\pi = 1332 \text{ cm}^{-1}$, identified by a black vertical line, and on the vertical axis we plot (a) the angle θ between the laser linear polarization and the crystallographic axis, going from $\theta = 0$ to 45° (due to the symmetry of the crystal, all other θ values will be related to this range), and (b) the laser bandwidth W , going from zero to $W = 190\gamma$, and where the value for our experiment $W = 24\gamma$ ($W = 264 \text{ cm}^{-1}$ or FWHM 70 cm^{-1}) is indicated by a black horizontal line. The thick red regions indicate the parameters where $E \rightarrow 1$, showing maximum entanglement.

Maximum entanglement occurs at $\theta = 0^\circ$, in a region below resonance close to 1200 cm^{-1} and another above, close to 1400 cm^{-1} . The measurements in Fig. 1 illustrate this for the 0° and 45° conditions, for which $|HH\rangle$ and $|VV\rangle$ are a Schmidt basis, and the balance between HH and VV counts reflects how close it is to maximum entanglement. At 0° the purely electronic response (VV) is strong, and maximum entanglement occurs where the HH response crosses it with the same amount of scattered photon pairs. Conversely, at 45° the purely electronic response (HH) is weak in comparison with the VV scattering, which contains the Raman response, thus making it impossible for the probability amplitude of the $|HH\rangle$ component to balance with the $|VV\rangle$ one, when it would reach a maximally entangled state.

If the laser bandwidth W grows, as shown in Fig. 2 (b), the shape of the resonance

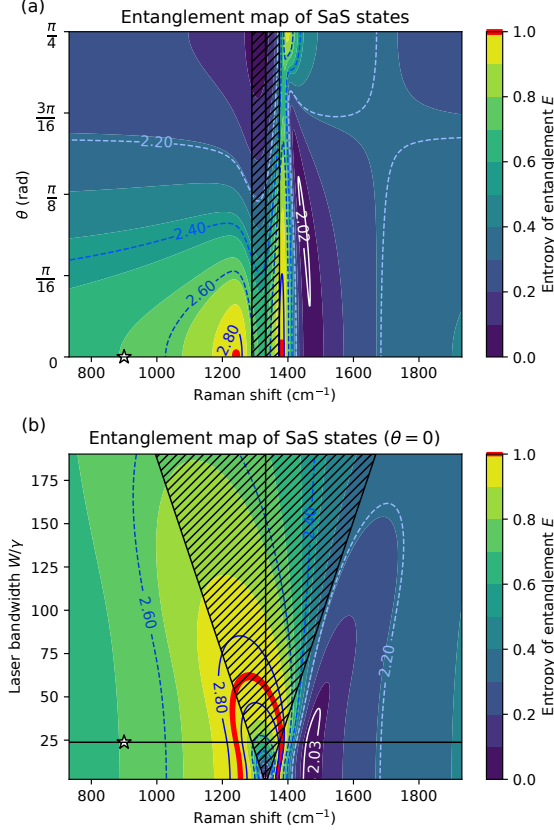


FIG. 2. Entanglement map for the SaS states in (a) the present experiment and (b) a generic centrosymmetric cubic system. In (a), the laser bandwidth W is fixed at $W = 264 \text{ cm}^{-1}$, the value of our experiment, as localized in (b) by a horizontal line. The black vertical line is the resonant Raman shift $\omega_{ph}/2\pi$, and the red regions mark the entanglement maxima ($E > 0.999$). As tensor components in Eq. (5) we used the values from table I. The star localizes the experiment of Ref. [12]. In blue shades, we plot contour curves for the Gisin parameter F . The hatched regions, within one laser bandwidth FWHM, indicates a high production of independent SaS photon pairs.

curve is smoothed out, so the ratio between the $|VV\rangle$ and $|HH\rangle$ coefficients gets more and more even along the SaS spectrum. Because of this, the entanglement extremes become less pronounced as W grows, until the point that it is not possible to reach maximum entanglement anymore, at $W \approx 70\gamma$. On the other hand, it also gets harder to obtain a separable state, which depends on a peak of either the $|VV\rangle$ or the $|HH\rangle$ component in relation to the other.

In Fig. 2 there is a hatched region indicating where the uncorrelated SaS pair production is high (low $g^{(2)}$ region in Fig. 1 (c,d)), corresponding to $2W$, around $1.2 \times \text{FWHM}$. In

this region, the scattered state is not properly represented by Eq. (2), but it needs to be complemented by non-FWM scattering events, which involves the scattering of real phonons, that happens within a laser bandwidth around the Raman resonance. Outside this region, though, state (2) is a good representation of the scattered SaS state, and our entanglement measure is representative.

To complete the analysis, we have also drawn level curves for the violation of Bell-type CHSH inequalities as a function of the light-matter parameters. These curves correspond to the so-called Gisin parameter F [19, 20] which, for pure states, reads $F = 2(1 - \mathcal{P})^{1/2}$, where $\mathcal{P} = 1 - \text{Tr}_i(\rho_i)^2$ is the linear entropy of either subsystem i . For separable states $F = 2$, which means that no separable state can go above the classical upper bound in the CHSH inequality, equal to 2. It reaches its maximum at $F = 2\sqrt{2} \approx 2.83$ for maximally entangled states. We plot the F parameter in Fig. 2 as blue shaded contour curves, and its smallest values within a white contour. Note that the maximal violation coincides with the maximally entangled states near 1200 cm^{-1} and 1400 cm^{-1} . Since Bell analysis is state dependent, and the generated $|\Psi_{SaS}\rangle$ state depends on the values of the light-matter parameters, the appropriate Bell angles to reach the maximum violation change for different regions of the map. As an example, the violation in the maximally entangled states near 1200 cm^{-1} is obtained for linear polarization angles $(0, \pi/4)$ for one of the photons and $(\pi/8, 3\pi/8)$ for the other, where the angles are in relation to V polarization.

Finally, we can localize the result of Ref. [12] in Fig. 2, represented by a white star. In the paper, it was found a state close to a Bell state at a symmetric Raman shift of 900 cm^{-1} with $\theta = 0^\circ$, with amplitude ratio of $|HH\rangle$ to $|VV\rangle$ at $\sqrt{0.28/0.72} \approx 0.62$. Calculating the ratio with our state (3) yields 0.49, and the discrepancy comes from our aS filter cutting some of the Raman contribution in HH at 900 cm^{-1} (left edge of Fig. 1 (a)), which does not happen in Ref. [12]. This region can be seen in the bottom left of Fig. 2 (a) and (b), where and $E \approx 0.7$ and $F \approx 2.5$.

To conclude, broadband polarization entanglement can be generated in four-wave mixing. The efficiency of the process can be controlled by how close the system is to the resonance with a Raman active phonon, and it is a matter of state engineering to choose the appropriate laser-crystal angle and SaS frequency in order to obtain a good balance between a good amount of entanglement and a sufficient pair production rate. The result is explored here for diamond, but it should be general for other centrosymmetric media, including silicon.

ACKNOWLEDGMENTS

This work was supported by IDOR/Pioneer Science Initiative (www.pioneerscience.org), CNPq (INCT-IQ 465469/2014-0, 302872/2019-1, 421469/2023-4, 307619/2023-0), FAPEMIG (APQ-01860-22, APQ-04852-23, RED0008123) and FAPERJ (CNE E-26/200.307/2023).

REFERENCES

* adojorio@fisica.ufmg.br

- [1] N. Bloembergen, *Nonlinear optics* (World Scientific Publishing Company, 1996).
- [2] R. W. Boyd, *Nonlinear optics* (Academic Press, 2008).
- [3] C. Shang and H. Hsu, The spatial symmetric forms of third-order nonlinear susceptibility, *IEEE Journal of Quantum Electronics* **23**, 177 (1987).
- [4] D. N. Klyshko, Correlation between the stokes and anti-stokes components in inelastic scattering of light, *Soviet Journal of Quantum Electronics* **7**, 755 (1977).
- [5] C. A. Parra-Murillo, M. F. Santos, C. H. Monken, and A. Jorio, Stokes–anti-stokes correlation in the inelastic scattering of light by matter and generalization of the bose-einstein population function, *Phys. Rev. B* **93**, 125141 (2016).
- [6] K. Thapliyal and J. Peřina Jr, Ideal pairing of the stokes and anti-stokes photons in the raman process, *Physical Review A* **103**, 033708 (2021).
- [7] K. C. Lee, M. R. Sprague, B. J. Sussman, J. Nunn, N. K. Langford, X.-M. Jin, T. Champion, P. Michelberger, K. F. Reim, D. England, *et al.*, Entangling macroscopic diamonds at room temperature, *Science* **334**, 1253 (2011).
- [8] K. Lee, B. Sussman, M. Sprague, P. Michelberger, K. Reim, J. Nunn, N. Langford, P. Bustard, D. Jaksch, and I. Walmsley, Macroscopic non-classical states and terahertz quantum processing in room-temperature diamond, *Nature Photonics* **6**, 41 (2012).
- [9] M. Kasperczyk, A. Jorio, E. Neu, P. Maletinsky, and L. Novotny, Stokes-anti-stokes correlations in diamond, *Opt. Lett.* **40**, 2393 (2015).
- [10] A. Saraiva, F. S. de A. Júnior, R. M. Souza, A. P. Pena, C. H. Monken, M. F. Santos, B. Koiller, and A. Jorio, Photonic counterparts of cooper pairs, *Physical Review Letters* **119**, 193603 (2017).

- [11] S. Timsina, T. Hammadia, S. G. Milani, F. S. de A. Júnior, A. Brolo, and R. de Sousa, Resonant squeezed light from photonic cooper pairs, *Physical Review Research* **6**, 033067 (2024).
- [12] T. A. Freitas, P. Machado, L. Valente, D. Sier, R. Corrêa, R. Saito, C. Galland, M. F. Santos, C. H. Monken, and A. Jorio, Microscopic origin of polarization-entangled stokes–anti-stokes photons in diamond, *Phys. Rev. A* **108**, L051501 (2023).
- [13] M. D. Levenson and N. Bloembergen, Dispersion of the nonlinear optical susceptibility tensor in centrosymmetric media, *Phys. Rev. B* **10**, 4447 (1974).
- [14] M. D. Levenson, C. Flytzanis, and N. Bloembergen, Interference of resonant and nonresonant three-wave mixing in diamond, *Phys. Rev. B* **6**, 3962 (1972).
- [15] F. S. de A. Júnior, A. Saraiva, M. F. Santos, B. Koiller, R. M. Souza, A. P. Pena, R. A. Silva, C. H. Monken, and A. Jorio, Stokes–anti-stokes correlated photon properties akin to photonic cooper pairs, *Phys. Rev. B* **99**, 100503(R) (2019).
- [16] B. J. Smith and M. G. Raymer, Two-photon wave mechanics, *Phys. Rev. A* **74**, 062104 (2006).
- [17] M. A. Nielsen and I. L. Chuang, *Quantum computation and quantum information* (Cambridge, 2010).
- [18] See supplemental material at [url will be inserted by publisher] for experimental and theoretical fitting details.
- [19] N. Gisin, Bell’s inequality holds for all non-product states, *Phys. Lett. A* **154**, 201 (1991).
- [20] A. Chefles and S. Barnett, Diagonalisation of the bell–chsh operator, *Phys. Lett. A* **232**, 4 (1997).